An Introduction to the Log-Polar Mapping

Helder Araujo

Department of Electrical Eng.
University of Coimbra
Coimbra, PORTUGAL 3030

Jorge M. Dias

Department of Electrical Eng.
University of Coimbra
Coimbra, PORTUGAL 3030

Abstract

One interesting feature of the human visual system is the topological transformation of the retinal image into its cortical projection. The excitation of the cortex can be approximated by a log-polar mapping of the eye's retinal image. In this tutorial paper we describe the log-polar mapping and its main properties.

1 Introduction

One interesting feature of the human visual system is the topological transformation ([Schwartz 84, Sandini *et al.* 80]) of the retinal image into its cortical projection. In our own human vision system, as well as in those of other animals, it has been found that the excitation of the cortex can be approximated by a log-polar mapping of the eye's retinal image. In other words, the real world projected in the retinas of our eyes, is reconfigured onto the cortex by a process similar to log-polar mapping before it is examined by our brain [Schwartz 84].

In the human visual system, the *cortical* mapping is performed through a space-variant sampling strategy, with the sampling period increasing almost linearly with the distance from the fovea. Within the fovea the sampling period becomes almost constant.This retino-cortical mapping can be described through a transformation from the *retinal plane* (ρ, θ) onto the *cortical plane* $(\log(\rho), \theta)$ as shown in figure 1. This transformation presents some interesting properties as scale and rotation invariance about the origin in Cartesian plane which are represented by shifts parallel to real and imaginary axis, respectively. This transformation is applied just on the $non-foveal$ part of a retinal image. If (x, y) are Cartesian coordinates and (ρ, θ) are the polar coordinates, by denoting $z = x + jy = \rho e^{j\theta}$ a point in the complex plane, the complex logarithmic (or log-polar) mapping is

$$w = ln(z). \qquad (1)$$

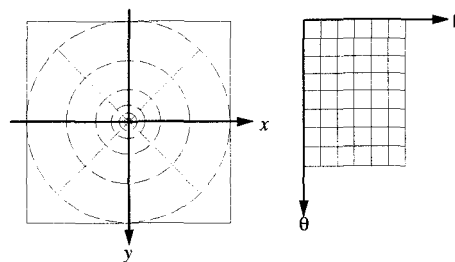for every $z \neq 0$ where $Real(w) = ln(\rho)$ and $Im(w) =$

Figure 1: Log-polar transformation. Any point (x_i, y_i) in the image plane (left) can be expressed in terms of (ρ, θ) in the cortical plane (right) by $(\ln_b(\rho), \theta)$.

$\theta + 2k\pi$. However we constrain angle θ to the range of $[0, 2\pi)$. This logarithmic mapping is a known conformal mapping preserving the angle of intersection of two curves.

1.1 Log-Polar Mapping and its Properties

Log-polar mapping can be performed from regular image sensors by using a space-variant sampling structure similar to the structure proposed in [Massone *et al.* 85]. This mapping is characterized by a linear relationship between the sampling period and the eccentricity ρ, defined as the distance from the image center. The figure 2 gives one example of these type of sampling structures.

The spatial variant geometry of the sampling points is obtained through a regular tesselation and a sampling grid formed by concentric circles with N_{ang} samples over each circle. The number of samples for each circle is always constant and they differ by the arc

$$\frac{2\pi}{N_{ang}}. \qquad (2)$$

between samples.

For a given N_{ang}, the radius ρ_r of the circle i is expressed by and an equation of the type
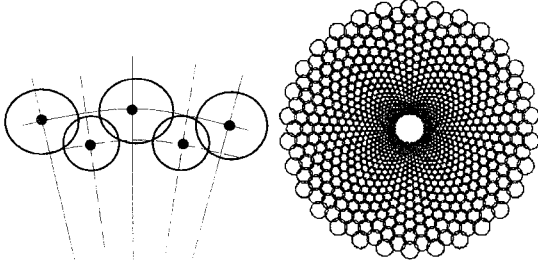
$$\rho_{r_i} = \rho_{fovea} b^i \qquad (3)$$

139

Figure 2: Graphical representation of the sampling structure. In this example the number of angular samples $N_{ang} = 60$. In this scheme the sampling point is shifted half sample period between consecutive circles.

with $i = 0..N_{circ}$ and $\rho_{fovea} > 0$ and representing the minimum radius of the sampling circles. The transformation for discrete entries of cortical plane is performed by using the following expressions

$$
\begin{aligned}
\rho_{ci} &= \ln_b \frac{\rho_{r_i}}{\rho_{fovea}} \\
\theta_{cj} &= \frac{\theta_{r_j}}{\Delta}
\end{aligned} \tag{4}
$$

with $\Delta = \frac{2\pi}{N_{ang}}$.

For the example illustrated in figure 2 the base b is

$$
b = \left(1 + \frac{\pi}{\sqrt{3}\, N_{ang}} \right) \tag{5}
$$

For different types of sampling strategies (different bases b) the concentric circles are always sampled with the period

$$
T_{ri} = \frac{2\pi \rho_{ri}}{N_{ang}} \tag{6}
$$

For the case where the base is expressed by (5) each sample covers a patch of the image corresponding to a circle with radius given by

$$
T_{radius} = \frac{2\pi \rho_{ri}}{3 N_{ang}}. \tag{7}
$$

The value for ρ_{fovea} could be chosen equal to the minimum sampling period to cover all the image center without generate oversampling in the retinal plane. If we want to obey to this constraint then

$$
\rho_{fovea} \geq \frac{N_{ang}}{2\pi} \tag{8}
$$

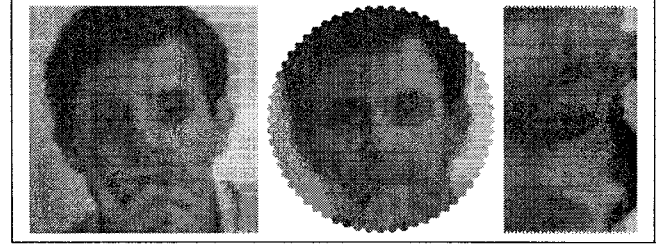In this sampling structure the angular sampling is shifted by half sampling period between successive

Figure 3: Example of images sampled by regular sampling structure and remapped by using a space-variant structure. The original image has 256×256 samples and the cortical plane has 71×60 samples.
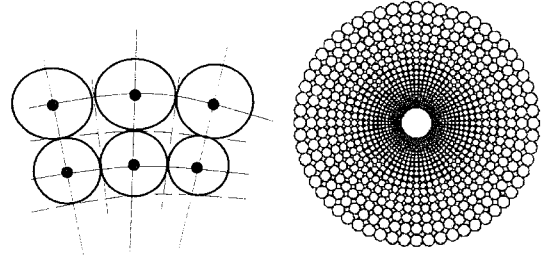

Figure 4: Graphical representation of a more simple sampling structure. The figure represents a structure with $N_{ang} = 60$ angular samples.

sampling circles and the expression θ_{r_i} for the equation is given by

$$
\theta_{ri} = \frac{2\pi}{N_{ang}} \left(j + \frac{odd(i)}{2} \right) \tag{9}
$$

where $j = 0..N_{ang}$.

Results from this kind of transformation are illustrated in figure 3. The intensity value in the cortical plane is obtained by the mean of the intensity values inside the circle centered at the sampling point (ρ_{ri}, θ_{ri}). That is the case of the images in figure 3.

This space-variant sampling structure can be modified for a more simplified sampling structure as it is illustrated in Figures 4 and 5. This simplified structure does not use as many samples as the structure described before and it is useful to speedup the algorithms based on this type of data sampling.

This structure is similar to the structure described above. The spatial variant geometry of the sampling points is also obtained through a tessellation and a sampling grid formed by concentric circles with N_{ang} samples over each circle. The number of samples for each circle is also constant and for a given N_{ang}, the radius basis b is expressed by
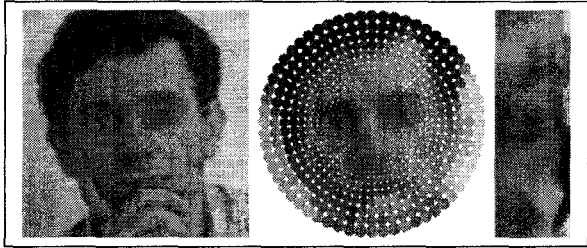
140

Figure 5: Example of images remapped in logpolar using the simplified version of sampling. The original images have 256×256 samples and the cortical plane only have 20×60 samples.

$$b = \frac{N_{ang} + \pi}{N_{ang} - \pi} \qquad (10)$$

with $i = 0..N_{circ}$ and ρ_{fovea} the minimum radius of the sampling circles. The radius ρ_r of the circle is expressed by

$$\rho_{r_i} = \rho_{fovea}\left(\frac{N_{ang} + \pi}{N_{ang} - \pi}\right)^i \qquad (11)$$

The concentric circles are sampled with the period described by the expression (2) and each sample covers a patch of the image corresponding to a circle with radius given by

$$T_{radius} = \frac{\pi \rho_{ri}}{N_{ang}}. \qquad (12)$$

The value ρ_{fovea} could be chosen equal to the minimum sampling period to cover all the image center without generating oversampling in the retinal plane. This constraint is expressed by

$$\rho_{fovea} \geq \frac{N_{ang}}{\pi} \qquad (13)$$

Examples of images sampled with this structure are shown in Figure 5. The intensity value at each point of the *cortical plane* are obtained by the mean of the intensity values inside the circle centered at the sampling point (ρ_{ri}, θ_{ri}). This image presents some gaps between the circles but a better result is obtained if the area around the sampling point is filled in.

This simplified version of space variant structure needs less storage then the first sampling structure, as we can verify in the Table 1

1.1.1 Log-Polar Properties

The log-polar mapping has number of important properties that make it useful as a sampling structure. The mapping of two regular patterns as shown in figure 6

	Reg. Samp.	Log-Polar
$b = \left(1 + \frac{\pi}{\sqrt{3}\,N_{ang}}\right)$	262144 samples	6540 samples
$b = \frac{N_{ang} + \pi}{N_{ang} - \pi}$	262144 samples	1860 samples

Table 1: Different sampling schemes also require different storage in memory.
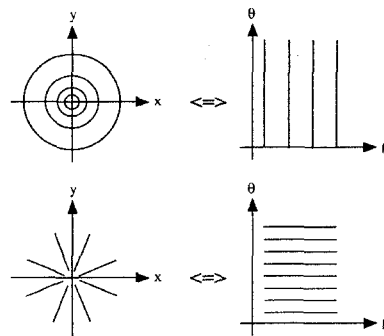

Figure 6: The log-polar mapping applied to regular patterns. (a) Applied to concentric circles in the *image* plane are mapped in vertical lines in the *cortical* plane. (b) Applied to radial lines in the *image* plane are mapped in horizontal lines in the *cortical* plane.

results in similarly regular patterns in the other domain. From the figure 6(a) the concentric circles in the image plane become vertical lines in the *cortical* plane. A single circle maps to a single vertical line since the constant radius r at all angles θ of the circle gives a constant ρ_c coordinate for all θ_c coordinates. Similarly an image of radial lines which have constant angle but variable radius, result in a map of horizontal lines.

These mapping characteristics are fundamental for some properties such as rotation and scaling invariance. Rotation and scaling result in shifts along the θ_c and ρ_c axis, respectively. For rotation invariance notice that all possible angular orientations of a point at given radius will map to the same vertical line. Thus, if an object is rotated around the origin, between successive images, this will result in only a vertical displacement of the mapped image. This same result is valid for radial lines. As a radial line rotates about the origin, its entire horizontal line mapping moves only vertically.

Scaling invariance is another characteristic of this log-polar mapping. From the figure 6(b) we seen that as point moves out from the origin along a radial line, its mapping stays on the same horizontal line mov-
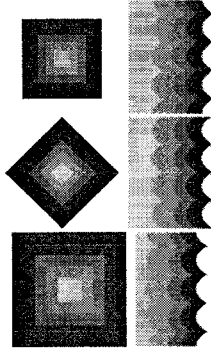
Figure 7: The effect of rotation and scaling with log-polar mapping. The original image in the left is rotated and scaled. The effect in the cortical plane is an image with similar shape with the edges at different position but equivalent to a circular shift in the cortical plane.
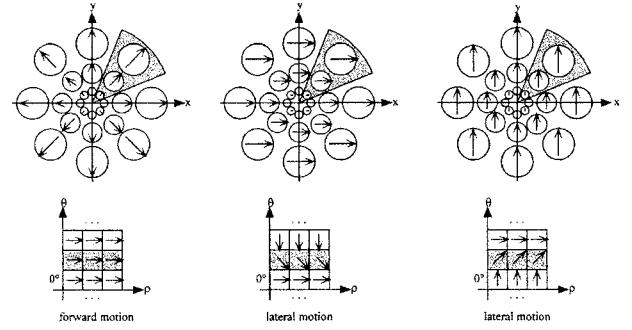

Figure 8: The optical flow vectors for different types of translational motion. For lateral motion the optical flow vectors generate in the cortical plane, stream lines of vectors with the same orientation. For forward motion these lines are equal in all the plane.

ing from the left to the right. The mappings of the concentric circles remain vertical lines and only move horizontally as the circles change in size.

The images of figure 7 illustrate these two properties. The original image is rotated and scaled and the images correspondent to the cortical planes before and after the transformation are similar. The edges have similar shape at position equivalent to a circular shift in the cortical plane. These properties were fundamental for the development of algorithms for pattern recognition [Reitboeck et al. 84], [Massone et al. 85].

Another property is related with projection of the images when the sensor translates. The images of Figure 8 show the mapping of the optic flow vectors for different types of translational motion of the sensor. Notice that when the sensor translates in same direction as the optical axis the optical flow generated appears as vectors diverging from the image center. The effect in the cortical plane is a set of lines with vectors with the same orientation, as illustrated in Figure 8.

1.2 Normal Optical Flow on Log-Polar

The space variant resolution and sampling exhibits interesting properties for the optical flow. In this point we study some of these properties of the optical flow.

The relate the optical flow field in log-polar coordinates with the 2D velocity field in cartesian coordinates let us write

$$
\begin{bmatrix} \dot{\rho} \\ \dot{\theta} \end{bmatrix} = \begin{bmatrix} \frac{\partial \rho}{\partial x} & \frac{\partial \rho}{\partial y} \\ \frac{\partial \theta}{\partial x} & \frac{\partial \theta}{\partial y} \end{bmatrix} \begin{bmatrix} \dot{x} \\ \dot{y} \end{bmatrix} \qquad (14)
$$

where $\dot{\rho}, \dot{\theta}, \dot{x}, \dot{y}$ stand for the derivatives with respect to time. Substituting the partial derivatives by their

expressions we obtain

$$
\begin{bmatrix} \dot{\rho} \\ \dot{\theta} \end{bmatrix} = \begin{bmatrix} \cos\theta & \sin\theta \\ -\frac{\sin\theta}{\rho} & \frac{\cos\theta}{\rho} \end{bmatrix} \begin{bmatrix} \dot{x} \\ \dot{y} \end{bmatrix} . \qquad (15)
$$

Defining

$$
\xi = \ln_b \frac{\rho}{\rho_{fovea}} \qquad (16)
$$

and $\gamma = \theta$, the relationship between the time derivatives of ξ and ρ is given by

$$
\dot{\xi} = \frac{1}{\ln b} \frac{\dot{\rho}}{\rho} = \frac{1}{\ln b} \frac{\dot{\rho}}{\sqrt{x^2 + y^2}}. \qquad (17)
$$

From (15) and using (17) we obtain the relationship between the motion field in Cartesian coordinates $(\dot{x}, \dot{y})$ and log-polar coordinates $(\dot{\xi}, \dot{\gamma})$ as

$$
\begin{bmatrix} \dot{\xi} \\ \dot{\gamma} \end{bmatrix} = \frac{1}{\sqrt{x^2 + y^2}} \begin{bmatrix} \frac{\cos\gamma}{\ln b} & \frac{\sin\gamma}{\ln b} \\ -\sin\gamma & \cos\gamma \end{bmatrix} \begin{bmatrix} \dot{x} \\ \dot{y} \end{bmatrix} . \qquad (18)
$$

The relative motion of the observer with respect to the scene gives rise to motion of the brightness patterns in the image plane. The instantaneous changes of the brightness pattern in the image plane are analyzed to derive the optical flow field, a two-dimensional vector field (u, v) reflecting the image displacements.

The optical flow value of each pixel is computed locally - that is, only information from a small spatio-temporal neighborhood is used to estimate it. In general, it is not possible to compute the true velocity of an image point just by observing a small neighborhood. Suppose that we are watching a feature (a piece of contour or a line) at two instants of time and through a small aperture smaller than the feature - see figure 9.
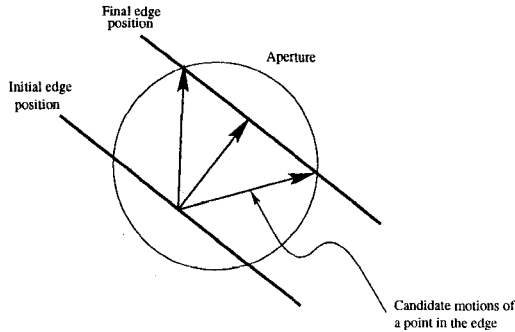
Figure 9: A line feature or contour observed through a small aperture at time t moves to a new position at time $t + \delta t$. In the absence of knowledge of camera motion, when we are looking at a viewpoint-independent edge in an image through an aperture, all we can say about the evolving image position of an indistinguishable point along the edges is that this position continues to lie somewhere along the evolving image of the edge.

Watching through this small aperture, it is impossible to determine where each point of the feature has moved to. The only information directly available from local measurements is the component of the velocity which is perpendicular to the feature, the *normal flow*. The component of the optical flow parallel to the feature can not be determined. This ambiguity, is known as the *aperture problem* and exists independently of the technique employed for local estimation of flow. However in cases where the aperture is located around an endpoint of a feature, the true velocity can be computed, because the exact location of the endpoint at two instants of time can be computed. Thus, the aperture problem exists in regions that have strongly oriented intensity gradients, and may not exist at locations of higher-order intensity variations, such as corners.

Any optical flow procedure involves two computational steps. In the first, assuming the local conservation of some form of information, only local velocity is computed. In a second step, in order to compute the other component of the optical flow vectors, additional assumptions have to be made.

The approach introduced by [Horn *et al.* 81] is based on the assumption that for a given scene point the intensity I at the corresponding image point remains constant over a short time instant. This corresponds to a brightness constancy assumption, $\frac{dI}{dt} = 0$, that gives a relationship that can be used to estimate the flow parameters directly from the spatial and temporal grey-level gradients. If a scene point projects

onto image point (ξ, γ) at time t and onto the image point $(\xi + \delta\xi, \gamma + \delta\gamma)$ at time $(t + \delta t)$ we obtain the optical flow constraint equation [Horn *et al.* 81],

$$\frac{\partial I}{\partial \xi} u + \frac{\partial I}{\partial \gamma} v + I_t = I_\xi u + I_\gamma v + I_t = 0. \tag{19}$$

which relates the flow (u, v) to the partial derivatives (I_ξ, I_γ, I_t) of the image I. From this constraint alone, without making any additional assumptions, we can only compute the normal flow u_n, equivalent to projection of optical flow on the gradient direction:

$$u_n = -I_t \frac{1}{\|\Delta I\|}. \tag{20}$$

Let $I(\xi, \gamma, t)$ denote the image intensity, and consider the optical flow field $\mathbf{v} = (u, v)$ and the motion field $\mathbf{v}_m = (u_m, v_m)$ at the point (ξ, γ), where the normalized local intensity gradient is $\mathbf{n} = (I_\xi, I_\gamma)/\sqrt{I_\xi^2 + I_\gamma^2}$. The normal motion field at point (ξ, γ) is by definition

$$u_{m_n} = \mathbf{v}^T \mathbf{n} = (\frac{d\xi}{dt}, \frac{d\gamma}{dt}) \cdot \frac{\Delta I}{\|\Delta I\|} = \frac{1}{\|\Delta I\|}(I_\xi \frac{d\xi}{dt}, I_\gamma \frac{d\gamma}{dt}). \tag{21}$$

If we approximate the differential $\frac{dI}{dt}$ by its total derivative we get a relation between the equations (20) and (21)

$$u_{m_n} - u_n = (\frac{1}{\|\Delta I\|} \frac{dI}{dt}). \tag{22}$$

which shows that the two fields are close to equal when the local image intensity gradient ΔI is high. This confirms that the normal flow is a good measurement of the normal motion field in locations where the intensity gradient exhibits high magnitude [Fermuller *et al.* 95].

References

[Aloimonos *et al.* 88] Y. Aloimonos, Y. Weiss, A. Bandopadhay, "Active Vision", *International Journal of Computer Vision*, Vol.7, 1988, pp. 333–356.

[Bailey *et. al* 90] J. G. Bailey and R. A. Messner, "Docking target design and spacecraft tracking system stability", in *SPIE - Intelligent Robots and Computer Vision VIII: Algorithms and Techniques*, Vol.1192, pp. 820–831, 1990.

[Bajcsy 88] R. Bajcsy, "Active Perception", *Proceedings of the IEEE*, Vol.76, August 1988, pp. 996-1005.

[Bederson *et al.* 92] B. B. Bederson, R. S. Wallace, and E. L. Schwartz, "A miniaturized active vision system", in *Proc. 11th IAPR International Conference on Pattern Recognition Vol. IV, Conference D: Architectures for Vision and Pattern Recognition*, pp. 58–61, 1992.

[Bederson *et al.* 94] B. B. Bederson, R. S. Wallace, and E. L. Schwartz, "A Miniaturized Space-Variant Active Vision System: Cortex-I", in *Artificial Neural Networks for Speech and Vision*, Richard J. Mammone, ed., pp. 429–456, Chapman and Hall, 1993.

[Bederson *et al.* 95] B. B. Bederson, R. S. Wallace, and E. L. Schwartz, "A miniaturized space-variant active vision system: Cortex-I", *Machine Vision and Applications*, Vol.8, pp.101-109, 1995.

[Carpenter 88] H. Carpenter, *Movements of the Eyes*, London, Pion Limited, 2nd edition.

[Coombs 92b] D. Coombs and C. Brown, "Real-time smooth pursuit tracking for a moving binocular robot", in *Proc. 1992 IEEE Comp. Soc. Conf. on Computer Vision and Pattern Recognition*, pp. 23–28, Champaign, USA.

[Fermuller *et al.* 95] C. Fermuller, Y. Aloimonos, "Qualitative Egomotion", *International Journal of Computer Vision*, Vol.15, 1995, pp. 7–29.

[Dias *et al.* 95] J. Dias, C. Paredes, I. Fonseca, J. Batista, H. Araújo, A. de Almeida, "Simulating Pursuit with Machines - Experiments with Robots and Artificial Vision", in *1995 IEEE Int. Conf. on Robotics and Automation*, Nagoya, Japan, May 1992.

[Horn *et al.* 81] B. Horn and B. Schunk, "Determining optical flow", *Artificial Intelligence*, Vol. 17, pp. 185-204, 1981.

[Manzotti *et al.* 94] R. Manzotti, R. Tiso, E. Grosso, G. Sandini, "Primary Ocular Movements Revisited", Technical Report 7/94, LIRA Lab, University of Genova, Italy, November 1994.

[Massone *et al.* 85] L. Massone, G. Sandini, V. Tagliasco, "Form-Invariant Topological Mapping Strategy for 2D Shape Recognition", *Computer Vision, Graphics, and Image Processing*, Vol. 30, 1985, pp. 169–189.

[Panerai *et al.* 95] F. Panerai, C. Capurro, G. Sandini, "Space Variant Vision for an Active Camera Mount", Technical Report TR 1/95, LIRA Lab, University of Genova, Italy, February 1995.

[Reitboeck *et al.* 84] H. Reitboeck and J. Altmann, "A model for size- and rotation- invariant pattern processing in the visual system", *Biological Cybernetics*, Vol. 51, 1984, pp. 113–121.

[Sandini *et al.* 80] G. Sandini, and V. Tagliasco, "A anthropomorphic retina-like structure for scene analysis", *Computer, Graphics and Image Processing*, Vol. 14, 1980, pp. 365–372.

[Hacisalihzade *et al.* 92] S. Hacisalihzade, L. Stark, J. Allen, "Visual Perception and Sequences of Eye Movement Fixations: A Stochastic Modeling Approach", *IEEE Trans. on Systems, Man, and Cybernetics*, Vol. SMC-22, No. 3, May/June 1992, pp. 474–481.

[Schwartz 84] E. Schwartz, "Anatomical and Physiological Correlates of Visual Computation from Striate to Infero-Temporal Cortex", *IEEE Trans. on Systems, Man, and Cybernetics*, Vol. SMC-14, No. 2, March/April 1984, pp. 257–271.

[Spiegel *et al.* 89] J. V. der Spiegel, G. Kreider, C. Claeys, I. Debusschere, G. Sandini, P. Belutti, and G. Soconi, "A foveated retina-like sensor using CCD technology", in *Analog VLSI Implementations of Neural Systems*, Carver Mead, ed., Boston, Kluwer, 1989.

[Wallace *et al.* 94] R. S. Wallace, P.-W. Ong, B. B. Bederson, E. L. Schwartz "Space Variant Image Processing", *Int. Journal of Computer Vision*, Vol. 13:1, pp.71–90, 1994.

[Weiman 88] C. F. Weiman, "Exponential sensor array geometry and simulation", in *Proc. SPIE Conf. on Pattern Recognition and Signal Processing*, Vol. 938, pp. 129–137, Orlando, 1988.

[Weiman 90] C. F. Weiman, "Video compression via log-polar mapping", in *Proc. SPIE Conf. on Real Time Image Processing II*, Vol. 1295, pp. 266–277, Orlando, 1990.

[Weiman 94] C. F. Weiman, *Log-Polar Binocular Vision System–Final Report*, SBIR Phase II Contract #NAS 9-18637, T.R.C., Danbury, December 1994.